Finite-Size Effects on the Structure of Grain Boundaries

E. A. Marquis, J. C. Hamilton, D. L. Medlin, and F. Léonard
Sandia National Laboratories, Livermore, California 94551, USA
(Received 3 May 2004; published 4 October 2004)

We present a combined experimental and theoretical analysis of the structure of finite-sized $\Sigma 3$ {112} grain boundaries in Au. High-resolution electron microscopy shows lattice translations at the grain boundary, with the magnitude of the translation varying *along* the finite-sized grain boundaries. The presence of this structural profile is explained using continuum elasticity theory and first-principles calculations as originating from a competition between elastic energy and the energy cost of forming continuous {111} planes across the boundary. This competition leads to a structural transition between offset-free and nontrivial grain boundary structures at a critical grain boundary size, in agreement with the experiments. We also provide a method to estimate the energy barrier of the γ surface.

DOI: 10.1103/PhysRevLett.93.156101 PACS numbers: 68.35.Ct, 61.72.–y, 68.35.Gy

Finite-size effects play a central role in physics, from the appearance of discrete energy levels in quantum dots to governing regimes of fluid flow. Recently, structural transitions driven by size, such as shape transitions of coherent precipitates [1] and magnetic phase transitions in ferroelectric nanosystems [2], have further highlighted the intriguing new physics that arises at reduced dimensionality. Since structure determines material properties, it is important to identify and understand these structural transitions. This is especially true for grain boundaries (GBs), specifically because grain boundary sliding is a significant deformation mechanism in polycrystalline materials, and is particularly sensitive to the detailed atomic structure of the grain boundary [3].

Here, we show that the structure of the $\Sigma 3$ {112} grain boundary provides a striking example of the importance of finite-size effects. Previous transmission electron microscopy works [4–7] have shown that this grain boundary can relax through a lattice translation. However, these studies, based on isolated observations of $\Sigma 3$ {112} boundaries, have painted a conflicting picture with reported translations ranging from zero to half the {111} plane spacing. Previously published computer simulations of the structure of the {112} grain boundary predict a translation as well, but ignore length effects by modeling infinitely long boundaries [6,8–10]. To address these issues, we have performed measurements on several grain boundaries of varying sizes in gold, allowing us to systematically study the role of the boundary size on its structure. By introducing a novel analysis of the high-resolution electron microscopy (HREM) images to extract the translation *along* the grain boundary, we identify a novel structural profile and discover a structural transition as a function of boundary length. This approach explains the discrepancies in the previously published results and provides a unified description of the $\Sigma 3$ {112} boundary. Furthermore, our analysis allows us to estimate, from the experimental data, the energy barrier of the γ surface, and we present first-principles calculations of the γ surface to support our findings.

Gold films were vapor deposited on polished and water etched ⟨110⟩-oriented NaCl crystal substrates maintained at 300 °C. After dissolving the substrate in water, free-standing specimens were placed on a Au fine-meshed grid and observed using a 4000-EX JEOL microscope operated at 400 kV. The films have a ⟨110⟩ texture with a high density of interconnected $\Sigma 3$ {111} and {112} grain boundaries. An example of a {112} boundary bounded by two {111} boundaries is shown in Fig. 1(a).

We are interested in the shift of the {111} planes along the y direction, i.e., parallel to the boundary plane, in the proximity of the grain boundary. The volume expansion sometimes associated with grain boundary relaxation [11] is not considered in this study. To extract the shapes of the {111} planes, the digitized HREM images are divided into bands (of width 1.62 Å corresponding to the {112} plane spacing), parallel to the y direction. For each band, the intensity is averaged over the x direction, and this average oscillates in y with a periodicity equal to d_0, the {111} plane spacing far from the {112} grain boundary. By fitting each local maximum with a sinusoidal function, the position of each {111} plane can be determined as a function of distance from the grain boundary. The {112} boundary plane is a glide-mirror plane, and it is placed unambiguously by reference to the kite unit [9] in all observed boundaries, as indicated in Fig. 1(b).

Such a measurement, shown in Fig. 1(c), indicates that {111} planes on opposite sides of the boundary bend in opposite directions, leading to an offset ϕ. The offset ϕ is not constant along the boundary but varies with y, $\phi = \phi(y)$. Figure 2 shows measurements of ϕ along two boundaries of length, $w = 32$ and 49 planes. The offset is small near the ends of the boundaries and reaches a maximum value at the center of the boundary. To understand the origin of this structure, we now propose a model for the finite-sized {112} boundaries.

The total energy of the boundary per unit length consists of two contributions, $E_{\text{tot}} = E_{\text{offset}} + E_{\text{elas}}$, where E_{offset} is the energy cost associated with the plane offsets

and given by the γ surface that represents the ground state energy of the interface as a function of the imposed translation [12], while E_{elas} is the elastic energy due to the offset. A model description of the offset energy is given by

$$E_{\text{offset}} = \frac{E_0}{2} \int \cos\left[\frac{2\pi\phi(y)}{d_0}\right] dy, \quad (1)$$

where E_0 is the barrier height per unit area and d_0 is the plane spacing ($d_0 = 0.23$ nm for the Au {111} plane spacing). The cosine shape is justified by a first-principles calculation described below.

The elastic contribution to the energy arises from the presence of a force dipole at the grain boundary. On each side of the boundary, there is an elastic restoring force that favors straight planes. Since the planes are bending in opposite directions on opposite sides of the boundary, the force changes direction across the boundary. From isotropic elasticity, the force in the y direction due to the elastic displacements $\mathbf{u}$ is

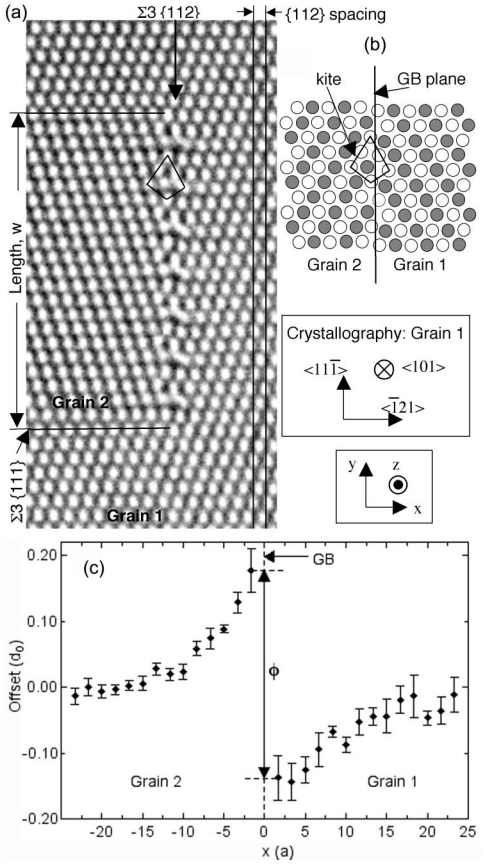

FIG. 1. (a) HREM image of a Au $\Sigma 3$ {112} boundary of length, w, equal to 22 {111} plane spacings and bounded by two $\Sigma 3$ {111} boundaries. (b) Embedded-atom method simulation of the grain boundary showing the characteristic kite feature. (c) Average of the y component of the displacement along six {111} planes in the middle of the boundary as a function of distance from the {112} boundary.

$$f_y = \left(K + \frac{4}{3}M\right)\frac{\partial \mu_{yy}}{\partial y} + \left(K - \frac{2}{3}M\right)\frac{\partial \mu_{xx}}{\partial y} + 2M\frac{\partial \mu_{yx}}{\partial x}, \quad (2)$$

where $\mu_{ij} = \frac{1}{2}(\partial_i u_j + \partial_j u_i)$, K is the bulk modulus, and M is the shear modulus. Because the ratio $(K + \frac{4}{3}M)/M \approx 7$ for Au (using the Voigt average for the elastic moduli [$K = \frac{1}{3}C_{11} + \frac{2}{3}C_{12}$, $M = \frac{1}{5}(C_{11} - C_{12}) + \frac{3}{5}C_{44}$ with published values for the C's [13]]), $\frac{\partial \mu_{yy}}{\partial y}$ is of the same order of magnitude as $\frac{\partial \mu_{xy}}{\partial x}$ [see Fig. 1(c) and Fig. 2 below], and, because there is no experimental evidence for significant displacements u_x, we neglect the last two terms in Eq. (2). Since u_y is largest near the GB, we model the force as a localized force near the GB,

$$f_y = \frac{\pi M d_0}{4(1-\sigma)} \frac{\partial^2 u_y}{\partial y^2}\bigg|_{x=a} [\delta(x-a) - \delta(x+a)]\mathbf{j}, \quad (3)$$

where $\mathbf{j}$ is a unit vector in the y direction, σ is the Poisson ratio, and a is the {112} plane spacing. [To obtain the magnitude of this localized force, we assumed a force dipole $\mathbf{f} = k(\partial^2 u_y/\partial y^2)|_{x=a}\frac{d\delta(x)}{dx}\mathbf{j}$ and calculated the resulting displacement vector $\mathbf{u}$ from $u_i(\mathbf{r}) = \int G_{il}(\mathbf{r} - \mathbf{r}')f_l(\mathbf{r}')d\mathbf{r}'$, where $G_{il}(\mathbf{r})$ is the Green's function for an infinite isotropic elastic medium [14]. The constant k was fixed by requiring that $\phi(y) = u_y(d_0, y) - u_y(-d_0, y)$.] The elastic energy per unit length is given by $E_{\text{elas}} = -\int f_y u_y dx dy$, and integration by parts gives the expression

$$E_{\text{elas}} = \frac{\pi M d_0}{2(1-\sigma)} \int |\nabla_y \phi|^2 dy. \quad (4)$$

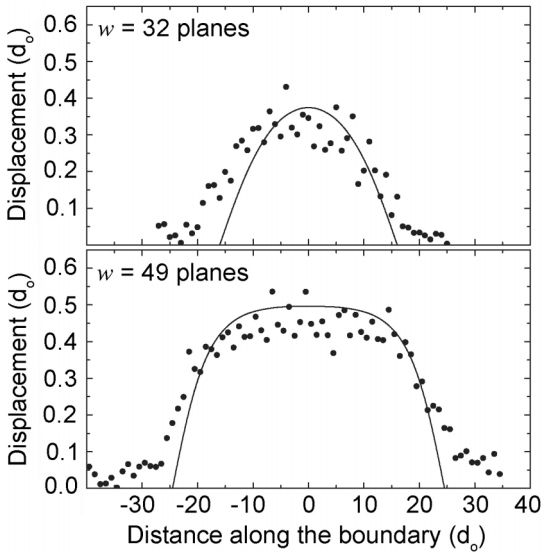

FIG. 2. Local displacement ϕ measured along two $\Sigma 3$ {112} grain boundaries of length $w = 32$ and 49 {111} plane spacings. The solid lines are least-squares fits using Eq. (7).

We define a parameter λ corresponding to the ratio of the energy scales of E_{elas} and E_{offset} as

$$\lambda = \frac{2\pi M d_0}{(1-\sigma)E_0}. \quad (5)$$

From the total energy $E_{\text{offset}} + E_{\text{elas}}$, one can now understand the structural profiles observed experimentally and shown in Fig. 2. In the absence of the elastic energy, the offset energy is minimized by $\phi = \pm\frac{d_0}{2}$, i.e., a constant half-plane offset across the boundary. However, because the offset must be small near the edges of the boundary, this constant ϕ profile leads to large gradients at the edges. In the presence of the elastic energy, such large gradients cost energy; hence the equilibrium profile is a compromise between E_{offset} and E_{elas}.

The profile $\phi(y)$ can be obtained by minimizing the total energy $\delta E_{\text{tot}}/\delta\phi = 0$, leading to the equation

$$-\frac{2\pi}{d_0}\sin\left(\frac{2\pi\phi}{d_0}\right) - \lambda\nabla^2\phi = 0, \quad (6)$$

with the assumption $\phi = 0$ at $y = \pm w/2$. This model does not take into account the nonzero offsets away from the boundaries (Fig. 2), which may result from elastic displacements and scatter in the experimental measurements. The solution is

$$\phi(y) = \frac{d_0}{\pi}\sin^{-1}[\beta\,\mathrm{sn}(\alpha,\beta)], \quad (7)$$

where $\alpha = \frac{2\pi}{d_0}\sqrt{1/\lambda}(\frac{w}{2} - |y|)$, $\beta = K^{-1}(\frac{\pi}{d_0}\sqrt{1/\lambda}w)$, $\mathrm{sn}(\alpha,\beta)$ is a Jacobi elliptic function, and $K^{-1}(x)$ is the inverse elliptical integral of the first kind [15].

We proceed to analyze our experimental data in the following way. For a given experimental boundary of length w, which is exactly the distance between the two $\Sigma3$ {111} boundaries, we perform a least-squares fit of Eq. (7) with the experimental data, for a range of values of λ. The solid lines in Fig. 2 show the best fits for two boundaries of length $w = 32$ and 49 d_o and with the best-fit values of λ equal to 1757 and 665, respectively. More generally, we have repeated the analysis for several boundaries of length between 18 and 60 plane spacings, and obtained an average value of $\lambda = 1044$, with a lower limit of 636 and an upper limit of 1757. Using Eq. (5) with the Voigt average for the elastic moduli and the best-fit values of λ, we obtain an estimate for the barrier height, $E_0 = 0.50\ \text{eV/nm}^2 \pm 0.24\ \text{eV/nm}^2$.

In order to confirm this estimate of the barrier height, we performed a first-principles calculation of the γ surface at $z = 0$ for the infinite $\Sigma3$ {112} boundary using a method similar to that described in Ref. [10]. We began by forming and relaxing infinitely long grain boundaries with offsets ranging from $-\frac{d_0}{2} < \phi < \frac{d_0}{2}$ and modeled with periodic boundary conditions. Our unit cell (59 atoms) was 2.95 Å × 7.23 Å × 61.9 Å in the $[11\bar{0}]$, [111], and $[11\bar{2}]$ directions, respectively. Along the $[11\bar{2}]$ direction, this cell contained 12 Å of vacuum, two $(11\bar{2})$ surfaces, and one $\{11\bar{2}\}$ grain boundary. We used the plane wave (cutoff energy = 230 eV) and the ultrasoft pseudopotential [16] based code, VASP [17]. The k-point sampling for the final calculation was $16 \times 8 \times 1$. Methfessel-Paxton smearing [18] of order one with a smearing width of 0.2 eV was used. The atomic configurations were relaxed until all atomic force components were <0.01 eV/Å. Minimum energy configurations for the boundary were found to lie at $\phi = \pm\frac{d_0}{2}$, which is in marked contrast to the Al $\Sigma3$ {112} boundary which has energy minima at $\phi \cong \pm\frac{d_0}{3}; \pm\frac{2d_0}{3}; \ldots$ [10]. Finally, the energy of intermediate offsets was calculated using the nudged elastic band method [19]. The results are shown in Fig. 3 along with the cosine model described above. The calculated energy barrier per unit area is $E_0 = 0.537\ \text{eV/nm}^2$. Convergence tests were performed as a function of k-point sampling, leading to the conclusion that this barrier is converged to within $\pm 0.02\ \text{eV/nm}^2$. The good agreement between our estimated and first-principles values of E_0 and the relatively narrow distribution of λ support the model description of the boundary energy. Our results also predict a high theoretical shear strength for the Au $\Sigma3$ {112} boundary, 1.1 GPa calculated from the maximum slope of the γ surface. This value is comparable to the Au theoretical shear strength, approximated by $\frac{M}{2\pi} \approx 4.8$ GPa [20], but much higher than the critical resolved shear strength of 0.9 MPa [21].

While the above discussion indicates that relatively long boundaries have a nontrivial structural profile, the competition between E_{elas} and E_{offset} leads to a structural transition for smaller boundaries. Figure 4 shows the measurements of the maximum displacement as a function of boundary length. A rapid increase in the maximum offset is observed for boundaries longer than ten plane spacings, with a saturation to about half a plane spacing for longer boundaries. As mentioned above, the curvature of the {111} planes is in opposite directions on opposite sides of the boundary plane [Fig. 1(a)] and the maximum offset is determined from the least-squares fits

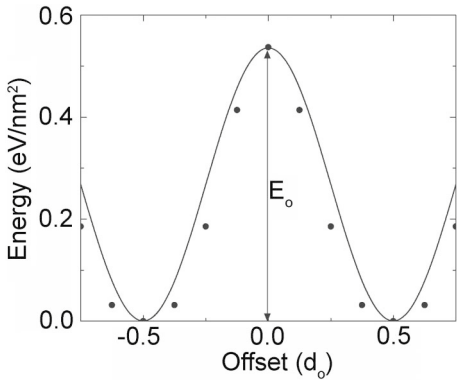

FIG. 3. Predicted grain boundary energy versus offset obtained from first-principles calculations. The solid line is the energy variation used for the analytical model.

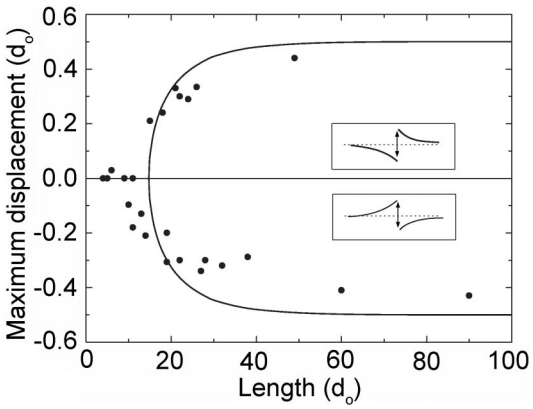

FIG. 4. Maximum local displacement versus grain boundary length. The solid line is obtained from Eq. (8) and $\lambda = 870$; see text for details.

described above. For short boundaries (fewer than about ten planes), however, the curvature of the {111} planes may be in the same direction on both sides of the {112} boundary due to constrained atomic relaxation, and, for these particular boundaries, the {111} plane offset is set to zero. By choosing the positive direction of the y axis when the kite unit is oriented as shown in Fig. 1(a) and the bottom {111} twin boundary is placed on the left side of the {112} boundary, ϕ is positive (negative) when the $x > 0$ side of the {112} boundary shifts upwards (downwards). Figure 4 shows that boundaries sample positive and negative offsets indicating that symmetry breaking occurs for the Au {112} boundary.

From the analytical model, we obtain the maximum offset as a function of length as

$$\phi_{\max} = \frac{d_0}{\pi} \sin^{-1}\left[K^{-1}\left(\pi \sqrt{\frac{1}{\lambda}} w \right) \right]. \tag{8}$$

Figure 4 shows the predicted behavior from this equation for $\lambda = 870$ [obtained from Eq. (4) and the first-principles value of E_0]. The general trend is reproduced, with a rapid rise of the maximum offset around 15 planes. For shorter grain boundaries, the predicted equilibrium structure is $\phi(y) \equiv 0$, i.e., no offset along the length of the boundary. Hence, there is a structural transition at a critical boundary length, from offset-free boundaries at short length to boundaries with nontrivial offset profiles for longer lengths. The presence of a transition can be understood by further analysis of Eq. (6). Near the transition point, the maximum offset is small, and the profile can be approximated as $\phi(y) = A \cos(\pi y/w)$, with $A \ll 1$; substitution in Eq. (6) leads to $A = (\sqrt{2} d_0/\pi) \times \sqrt{1 - \lambda d_0^2/4w^2}$. The solution is real as long as

$$w > \frac{\sqrt{\lambda} d_0}{2} = w^*, \tag{9}$$

defining the threshold length w^*. For $\lambda = 870$, the threshold length is $w^* = 15$ plane spacings, as shown in Fig. 4. For lengths $w < w^*$, the elastic energy is too costly to sustain any sort of offset structure.

In summary, we have shown that finite-size effects play a strong role in grain boundary physics, leading to a structural transition as a function of grain boundary size. The analysis presented here is general and could be applied to identify and study structural transitions in other grain boundary materials.

We thank U. Dahmen and N. Bartelt for useful discussions. This work was supported by the Office of Basic Energy Sciences, Division of Materials Sciences, U.S. Department of Energy, Contract No. DE-AC04-94AL85000.

[1] W. C. Johnson and J. W. Cahn, Acta Metall. **32**, 1925 (1984).
[2] C. L. Wang and S. R. P. Smith, J. Phys. Condens. Matter **7**, 7163 (1995).
[3] A. P. Sutton and R. W. Balluffi, *Interfaces in Crystalline Materials* (Oxford University Press, New York, 1996).
[4] W. Krakow and D. A. Smith, Ultramicroscopy **22**, 47 (1987).
[5] H. Ichinose, Y. Ishida, N. Baba, and K. Kanaya, Philos. Mag. A **52**, 51 (1985).
[6] D. L. Medlin, M. J. Mills, W. M. Stobbs, M. S. Daw, and F. Cosandey, Mater. Res. Soc. Symp. Proc. **295**, 91 (1993).
[7] J. M. Pénisson, U. Dahmen, and M. J. Mills, Philos. Mag. Lett. **64**, 277 (1991).
[8] R. C. Pond and V. Vitek, Proc. R. Soc. London A **357**, 453 (1977).
[9] U. Wolf, P. Gumbsch, H. Ishinose, and H. F. Fischmeister, J. Phys. (Paris), Colloq. **51**, C359 (1990).
[10] J. C. Hamilton and S. M. Foiles, Phys. Rev. B **65**, 064104 (2002).
[11] J. M. Pénisson and T. Vystavel, Ultramicroscopy **90**, 163 (2002).
[12] V. Vitek, Philos. Mag. **18**, 773 (1968).
[13] *CRC Handbook of Chemistry and Physics*, edited by D. R. Lide (CRC Press, Boca Raton, FL, 2003), 83rd ed.
[14] L. D. Landau and E. M. Lifshitz, *Theory of Elasticity* (Pergamon Press, New York, 1970), 2nd ed.
[15] Numerical routines for calculating these functions can be found in, for example, W. H. Press *et al.*, *Numerical Recipes in Fortran 77: The Art of Scientific Computing* (Cambridge University Press, Cambridge, 2001).
[16] D. Vanderbilt, Phys. Rev. B **41**, 7892 (1990).
[17] G. Kresse and J. Furthmuller, Phys. Rev. B **54**, 11 169 (1996).
[18] M. Methfessel and A. T. Paxton, Phys. Rev. B **40**, 3616 (1989).
[19] H. Jònsson, G. Mills, and K. W. Jacobsen, in *Classical and Quantum Dynamics in Condensed Phase Simulations*, edited by B. J. Berne, G. Ciccotti, and D. F. Coker (World Scientific, Singapore, 1998).
[20] J. P. Hirth and J. Lothe, *Theory of Dislocations* (Wiley, New York, 1982), 2nd ed.
[21] R. E. Reed-Hill and R. Abbaschian, *Physical Metallurgy Principles* (PWS-Kent, Boston, 1992), 3rd ed.